coatings

MDPI

Article

Effect of Co Contents on Microstructure and Cavitation Erosion Resistance of $NiTiAlCrCo_xN$ Films

Hongjuan Yan *, Fangying Cheng, Lina Si, Ye Yang, Zhaoliang Dou and Fengbin Liu

School of Mechanical and Materials Engineering, North China University of Technology, Beijing 100144, China; fangy0111@163.com (F.C.); silina_thu@163.com (L.S.); yangye@ncut.edu.cn (Y.Y.); dzl@ncut.edu.cn (Z.D.); fbliu@ncut.edu.cn (F.L.)

* Correspondence: yanhongj@sina.com

Abstract: In order to investigate the effect of Co contents on the structure and cavitation erosion property, $NiTiAlCrCo_xN$ films were prepared by the magnetron sputtering system. The X-ray diffractometer (XRD), the scanning electron microscope (SEM) and the energy dispersive spectrometer (EDS) were used to characterize the structure and morphology of the films. The nanoindenter and the scratch tester were used to analyze the mechanical properties of the films. Cavitation erosion experiments were carried out by the ultrasonic vibration cavitation machine. The results show that $NiTiAlCrCo_xN$ films with different Co contents have a simple face-centered cubic (FCC) structure and show a preferred orientation on the (200) crystal plane. The diffraction angle on the (200) crystal plane decreases and the interplanar spacing increases with the increase in Co content in $NiTiAlCrCo_xN$ films. $NiTiAlCrCo_xN$ films exhibit a typical columnar crystalline structure. With the increase in Co content, the nanohardness of the films increases and the elastic modulus of the films decreases, while the mass loss of cavitation erosion monotonously increases except for the film with a 1.2 Co molar ratio. The $NiTiAlCrCo_{1.4}N$ film has a minimum hardness of 13.264 GPa, a maximum elastic modulus of 253.22 GPa and a minimum mass loss of 0.72 mg in the cavitation erosion experiment. The $NiTiAlCrCo_{1.4}N$ film exhibits the best cavitation corrosion resistance because the addition of the Co element enhances the solid solution strengthening effect and the $NiTiAlCrCo_{x1.4}N$ film with the biggest elastic modulus has better elasticity to reduce the micro jet impact.

Keywords: $NiTiAlCrCo_xN$ film; Co contents; cavitation erosion; hardness

check for updates

Citation: Yan, H.; Cheng, F.; Si, L.; Yang, Y.; Dou, Z.; Liu, F. Effect of Co Contents on Microstructure and Cavitation Erosion Resistance of $NiTiAlCrCo_xN$ Films. *Coatings* **2024**, *14*, 603. https://doi.org/10.3390/coatings14050603

Academic Editors: Marin Kurtela and Biserka Runje

Received: 16 April 2024
Revised: 8 May 2024
Accepted: 8 May 2024
Published: 10 May 2024

1. Introduction

Cavitation erosion is one of the main factors causing the failure of key parts such as ship propellers and turbine blades [1]. Coating is widely used to improve the cavitation erosion resistance of parts [1,2]. The high-entropy alloy film is a new material with high hardness, corrosion resistance [1,2], oxidation resistance [3], wear resistance [4,5] and corrosion resistance [6–9]. Nonmetallic elements such as C, N and O were doped into high-entropy alloys to form high-entropy nitride or carbide films, which have better properties than high-entropy alloy films and can be used to improve the cavitation erosion resistance of parts [10–13]. In high-entropy ceramic films, the metal elements share cation positions and the nonmetallic elements occupy anionic positions, which forms a new material system and has a unique microstructure [11,14]. Researchers studied the effect of deposition parameters on film properties [15–20]. With the increase in bias potential on the substrate, the hardness of (TiZrHfVNb)N coatings increases. With the increase in working gas pressure, the hardness of (TiZrHfVNb)N decreases [12]. With the increase in the N_2:Ar flow ratio, (AlCrTiZrV)N high-entropy alloy nitride film exhibits the preferred orientation on the (200) crystal plane. The hardness and modulus firstly increase and then decrease [21,22]. Our group studied the effect of a N_2:Ar flow ratio on the cavitation erosion resistance of NiTiAlCrN films. The results show that, when the N_2:Ar flow ratio is 1:1, the NiTiAlCrN

films have the best cavitation erosion resistance [23]. The researchers also studied the effect of the elements on the structure and properties of HEAs [24–29]. The CoCrFeNiAl coating shows a BCC structure accompanied by a small amount of FCC and $AlCrO_3$ phase. The CoCrFeNiMn coating shows an FCC structure and a large amount of $MnCr_2O_4$ phase. The wear resistance of CoCrFeNiMn coating is better than the one of CoCrFeNiAl coating [26]. With the increase in x, the structures of $CoCrFeNiAl_xMn_{(1-x)}$ high-entropy alloy (HEA) coatings changes from an FCC structure to dual-phase FCC + BCC structure to BCC structure. The $CoCrFeNiAl_{0.8}Mn_{0.2}$ HEA coating with an FCC + BCC structure has the best corrosion resistance [27]. The $FeCoCr_xNiAl$ HEA coatings have a dual phase of FCC and BCC. The $FeCoCr_{1.5}NiAl$ coating has the highest hardness and the best wear resistance and corrosion resistance because the Cr element promotes the formation of a hard phase and a dense oxide film is formed in 3.5 wt.% NaCl solution [28]. With the increase in Si contents, the (AlCrTiZrMo)-Si_x-N high-entropy films with Si contents change from crystal to amorphous phases and the hardness and modulus first increase and then decrease [29]. Therefore, the content of the element can change the structure and improve the properties of the films. The cavitation erosion can cause phase transformations in Co alloys and Co shows superior cavitation erosion resistance in 304 and 316 stainless steel [30]. Therefore, Co plays a crucial role in the cavitation erosion of films.

The N_2:Ar flow ratio has been determined in our previous research. On this basis, the $NiTiAlCrCo_xN$ films with different Co contents were deposited by a magnetron sputtering system. The effect of Co contents on the microstructure, nanohardness, elastic modulus and cavitation erosion resistance of the $NiTiAlCrCo_xN$ films are studied.

2. Materials and Methods

2.1. Materials

The 304 stainless steel (Juncheng Co., Ltd., Tianjin, China) is a widely used chromium–nickel stainless steel. Therefore, it is selected as the substrate, which is mirror-polished. The element contents of 304 stainless steel are shown in Table 1. The dimensions of the substrate are Φ20 mm × 3 mm.

Table 1. Element contents of 304 stainless steel.

Elements	Fe	Cr	Ni	Mn	Si	C	S	P
Contents/wt.%	67~71	17~19	8~11	≤2.0	≤1.0	≤0.08	≤0.03	≤0.035

According to the definition of the high-entropy alloys, the content of every element ranges from 5 at.% to 35 at.%. Therefore, $NiTiAlCrCo_x$ alloys with a Co molar ratio of 0.6, 0.8, 1, 1.2 and 1.4 are selected as targets. The contents of Ni, Ti, Al and Cr in $NiTiAlCrCo_x$ targets are in equimolar ratios. The $NiTiAlCrCo_x$ targets are fabricated by powder metallurgy technology with a temperature of 900 °C and a pressure of 40 MPa. The purity of the targets is 99.99%. The dimensions of the targets are Φ50.4 mm × 4 mm.

2.2. Film Deposition

The $NiTiAlCrCo_xN$ films with different Co contents were deposited on 304 stainless steel by the magnetron sputtering system. The vacuum degree of the chamber is pumped to 3×10^{-3} Pa. The target was pre-sputtered for 15 min to clear impurities and oxide in the target surface. The surface impurities and oxide of the substrate were etched by Ar+. The nitrogen argon flow ratio was 3:4. In order to strengthen the adhesive strength between the substrate and $NiTiAlCrCo_xN$ film, the TiN layer was deposited for 60 min on the substrate. The $NiTiAlCrCo_x$ target was controlled by a DC power of 110 W. The $NiTiAlCrCo_xN$ films with different Co contents were deposited by changing the $NiTiAlCrCo_x$ targets with a different Co molar ratio. The deposition time was 180 min and the thickness of $NiTiAlCrCo_xN$ film is about 2 μm.

2.3. Film Characterization

The microstructures of the NiTiAlCrCo$_x$N films were analyzed by Rigaku Ultima IV X-ray diffraction (Tokyo, Japan) with Cu-Kα, a wavelength of 0.154 06 nm, a current of 40 mA, a voltage of 40 kV, a test step of 0.02°, a scanning speed of 8°·min^{-1} and an angle range from 10° to 80°. The surface and cross-section morphologies of NiTiAlCrCo$_x$N films and the wear track were analyzed with a Cart Zeiss Sigma-300 scanning electron microscope (SEM). The chemical compositions of NiTiAlCrCo$_x$N films and the wear track were analyzed with the Ultim Max energy spectrometer (Oberkochen, Germany) (EDS). The nanohardness and elastic modulus of NiTiAlCrCo$_x$N films were measured with the Anton Parr UNHT nanoindenter (Graz, Austria) with a Berkovich indenter (Graz, Austria), which has a curvature radius of the tip of 100 nm, a maximum load of 40 mN and loading and unloading rates of 20 mN·min^{-1}, with an indentation depth of 300 nm. A total of 5 points were selected to test the nanohardness and elastic modulus. The adhesive force of the NiTiAlCrCo$_x$N film was measured with a WS-2005 automatic scratch meter (Zhongke Kaihua Technology Co., Ltd., Lanzhou, China) with a load of 30 N, a loading rate of 30 N·min^{-1} and a scratch length of 3 mm. The scratch test was repeated 3 times in every sample. The cavitation erosion experiment was carried out with the ultrasonic vibration cavitation machine with a power of 1200 kW and an amplitude of 25 μm, which is shown in Figure 1. The diameter of the vibrating head was Φ20 mm. The 3.5 wt.% NaCl solution was selected as the cavitation erosion medium. The distance between the sample surface and the vibrating head was 0.5 mm. The ice was added into the circulating water in the bath to keep the samples at 0 °C. The sample was taken out and the mass loss of the sample was measured with a high-precision electronic balance for every 2 h of the cavitation erosion experiment. The total duration of the cavitation erosion experiment was 12 h. The cavitation rate is defined as the mass loss per hour. The cavitation erosion experiment was repeated 3 times for every NiTiAlCrCo$_x$N film.

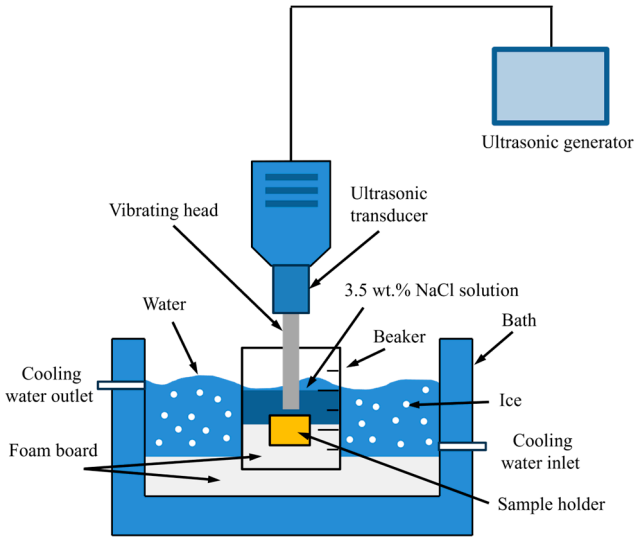

Figure 1. Diagram of the ultrasonic cavitation erosion machine.

3. Results and Discussion

3.1. Film Structure

Figure 2 shows the XRD patterns of NiTiAlCrCo$_x$N films with different Co contents. The films exhibit a face-centered cubic (FCC) structure and have a preferred orientation on the (200) crystal plane. The phases consist of TiN, AlN, CrN, Co_3Ti and $Co_{5.47}N$. When the molar ratio of Co in the targets is bigger than 1.0, the diffraction peak of (111) plane disappears. The diffraction angle on the (200) crystal plane shifts to the bigger angle and the interplanar spacing decreases with the increase in Co contents.

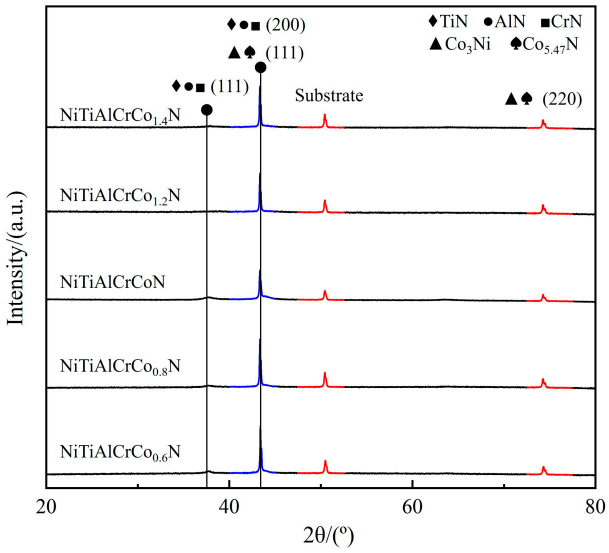

Figure 2. XRD patterns of NiTiAlCrCo$_x$N films.

Table 2 shows the diffraction angle, the interplanar spacing and the full-width half of the maximum (FWHM) on the (200) crystal plane. Except for the NiTiAlCrCoN film with equimolar ratios, the diffraction angle decreases and the interplanar spacing increases with the increasing of Co content. But the NiTiAlCrCoN film with equimolar ratios has the maximum diffraction angle and FWHM and the minimum interplanar spacing, which means that the NiTiAlCrCoN film has higher crystallinity and a finer grain size. The reason for this is that the film with equimolar ratios has the lattice distortion effect and the slow diffusion effect.

Table 2. Diffraction angle, interplanar spacing and FWHM.

Co Content	Diffraction Angle 2θ/(°)	Interplanar Spacing *d*/nm	FWHM *B*/rad
NiTiAlCrCo$_{0.6}$N	43.399	2.0833	0.119
NiTiAlCrCo$_{0.8}$N	43.342	2.0859	0.152
NiTiAlCrCoN	43.381	2.0842	0.193
NiTiAlCrCo$_{1.2}$N	43.340	2.0860	0.122
NiTiAlCrCo$_{1.4}$N	43.338	2.0861	0.115

With of the increase in Co content, the FWHM of NiTiAlCrCo$_x$N films first increases and then decreases, which means that the Co element can improve the peak quality. When the Co element is in an equimolar ratio, the peak quality of the XRD pattern is the best. The NiTiAlCrCoN film with equimolar ratios is more likely to generate multicomponent crystals in an alloy structure, which greatly increases entropy value and easily generates a crystal structure. Due to the different sizes of each atom in the site, the lattice position changes and the lattice distortion is intensified, which reduces the diffraction peak intensity and increases the FWHM of the NiTiAlCrCoN film on the (200) crystal plane. The NiTiAlCrCo$_x$N films with unequal molar ratios have a lower entropy which weakens the unique microstructure caused by the "cocktail" effect. Therefore, the NiTiAlCrCoN film with equimolar ratios exhibits specificity in XRD patterns.

3.2. Morphology

Figure 3 shows the elements map, the surface and the cross-section morphologies of the NiTiAlCrCo$_x$N films with different Co contents. The NiTiAlCrCo$_x$N films exhibit the typical columnar crystalline structure which is perpendicular to the substrate. The morphologies are sequentially the NiTiAlCrCo$_x$N layer, the TiN transition layer and the

substrate from top to bottom. The interfaces between layers are clear. The surface is smooth, flat, with no pores and no peel.

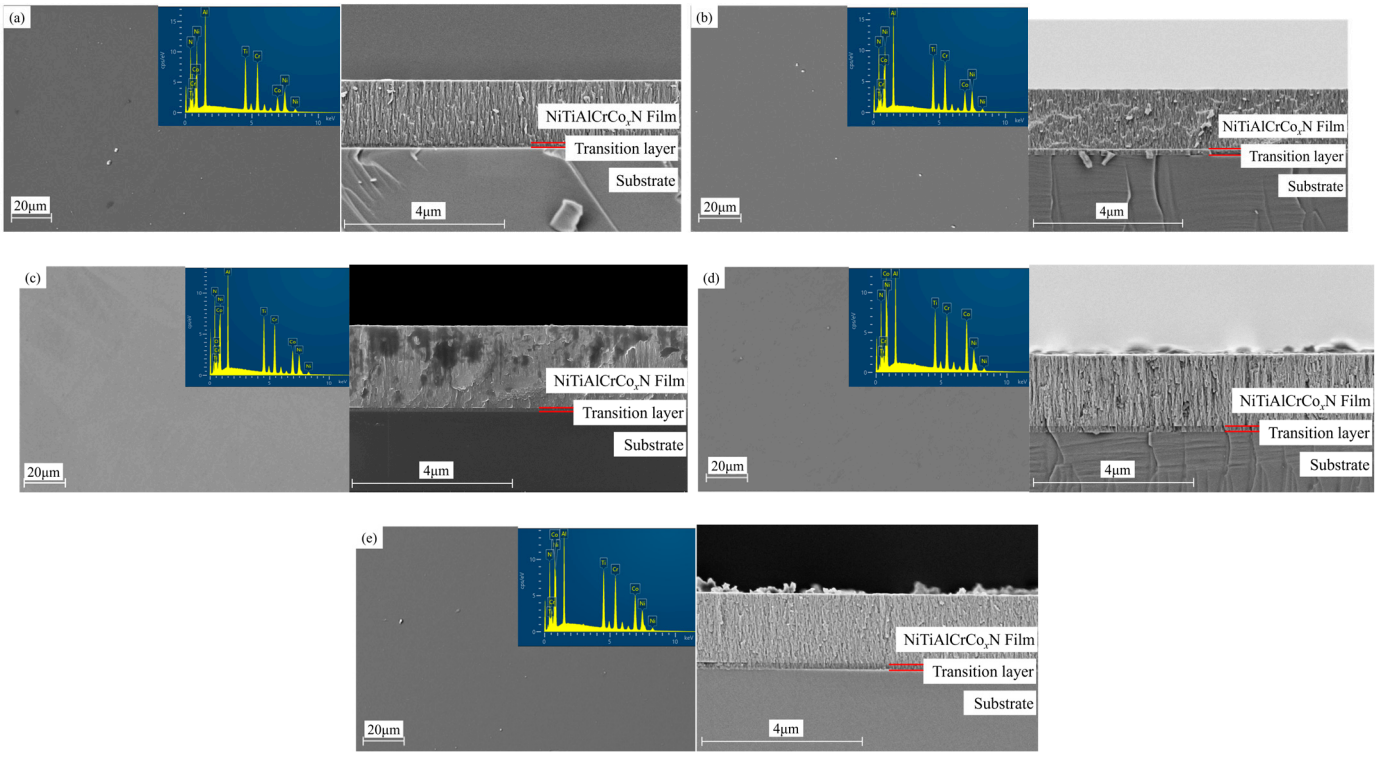

Figure 3. Element map, surface and cross-section morphologies of NiTiAlCrCo$_x$N films. (**a**) NiTiAlCrCo$_{0.6}$N; (**b**) NiTiAlCrCo$_{0.8}$N; (**c**) NiTiAlCrCoN; (**d**) NiTiAlCrCo$_{1.2}$N; (**e**) NiTiAlCrCo$_{1.4}$N.

Table 3 and Figure 4 show the element contents of NiTiAlCrCo$_x$N films with different Co contents, which was observed by EDS. The N contents in NiTiAlCrCo$_x$N films are about (39 $\pm$ 0.6) in percentage. The Co contents in NiTiAlCrCo$_x$N films increase from 9.4% to 22.53% with an increase in the Co molar ratio in the NiTiAlCrCo$_x$ targets. The other elements such as Ni, Ti, Al and Cr in NiTiAlCrCo$_x$N films are approximately equal.

Table 3. Element contents in NiTiAlCrCo$_x$N films.

	Ni	Ti	Al	Cr	Co	N
NiTiAlCrCo$_{0.6}$N	14.85	10.92	11.56	14.59	9.4	38.68
NiTiAlCrCo$_{0.8}$N	13.86	10.7	11.36	13.82	10.72	39.54
NiTiAlCrCoN	12.15	10.64	12.16	13.29	11.88	39.88
NiTiAlCrCo$_{1.2}$N	11.52	9.6	10.86	11.37	17.89	38.76
NiTiAlCrCo$_{1.4}$N	10.35	8.21	9.05	10.74	22.53	39.12

Figure 5 shows the element distribution of point scanning, which was taken five points from top to bottom in the cross-section of the NiTiAlCrCo$_x$N film. In the NiTiAlCrCo$_{0.6}$N film, the metal elements are more easily concentrated near the substrate and the N element increases from bottom to top, which increases the nitride content near the surface. With the increase in Co content in the NiTiAlCrCo$_{1.4}$N film, the metal elements increase and the N element decreases near the surface. The solid solution strengthening effect increases significantly between metal elements and nitrides near the substrate, resulting in an increase in nitrides near the substrate.

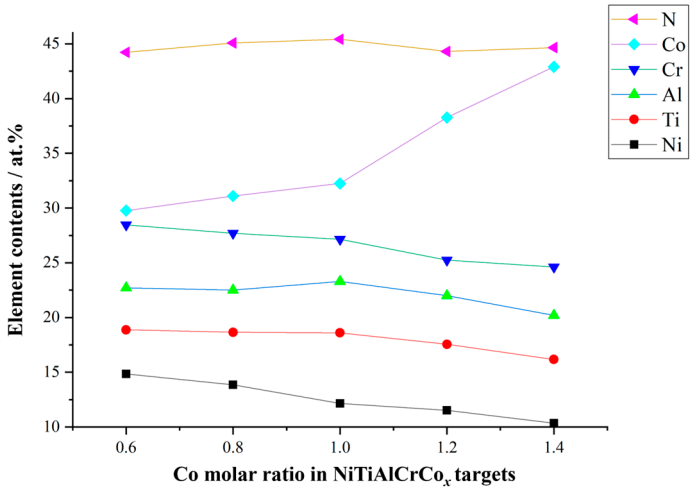

Figure 4. Element contents in NiTiAlCrCo$_x$N films.

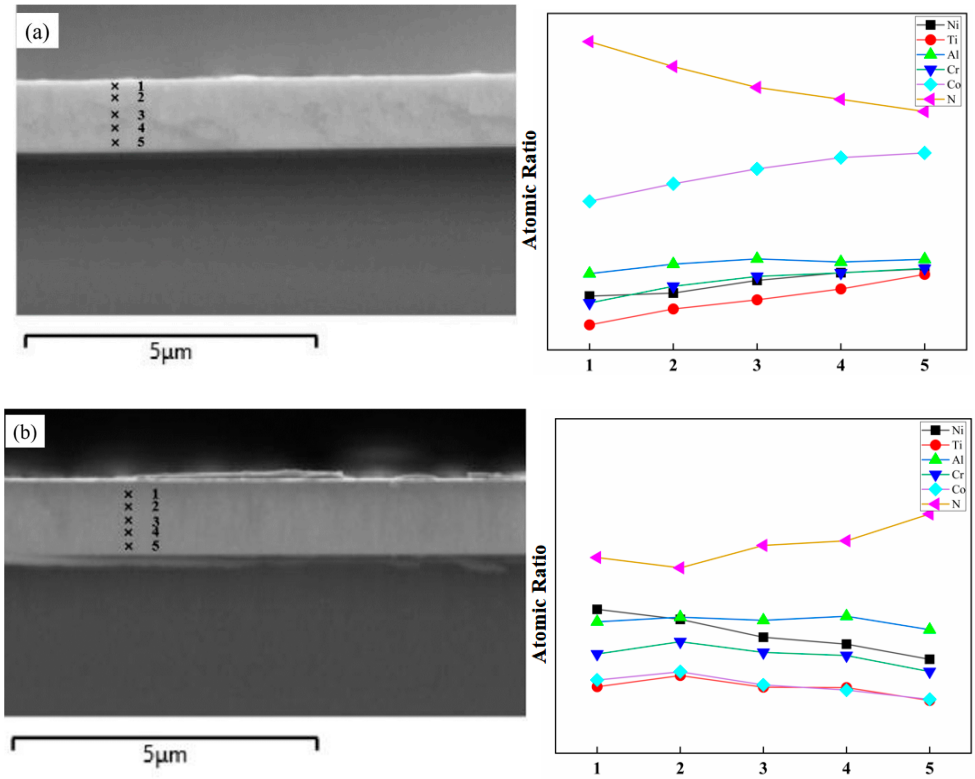

Figure 5. Element distribution in cross-section of NiTiAlCrCo$_x$N films (the numbers of 1, 2, 3, 4, 5 in cross-section are the position of the point scanning). (**a**) NiTiAlCrCo$_{0.6}$N; (**b**) NiTiAlCrCo$_{1.4}$N.

3.3. Mechanical Properties

Figure 6 shows the average nanohardness and the elastic modulus of NiTiAlCrCo$_x$N films. With the increase in Co content, the nanohardness of the NiTiAlCrCo$_x$N films decreases and the elastic modulus of the NiTiAlCrCo$_x$N films increases, expect for the ones of the NiTiAlCrCo$_{1.2}$N film. When the Co molar ratio is 1.4, the film has a minimum hardness of 13.264 GPa and a maximum elastic modulus of 253.22 GPa. When the Co molar ratio is 0.6, the film has a maximum hardness of 14.178 GPa and a minimum elastic modulus of 229.40 GPa.

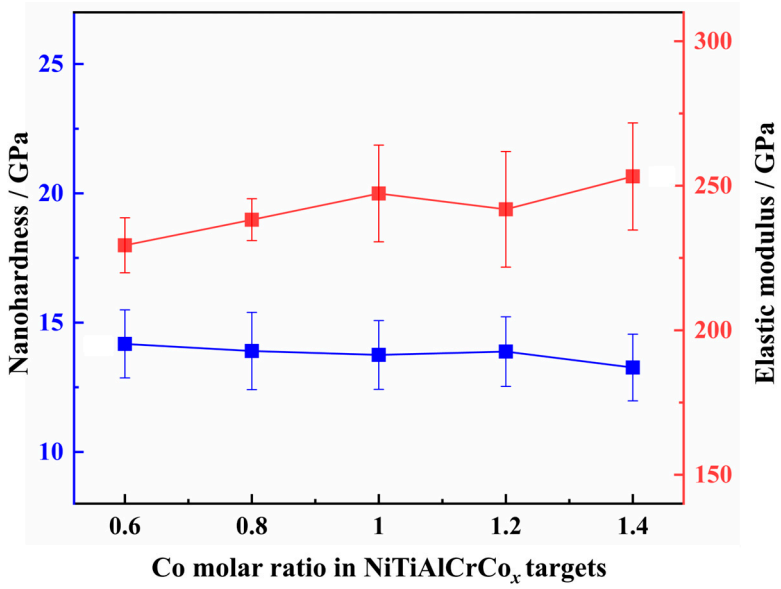

Figure 6. Nanohardness and elastic modulus of NiTiAlCrCo$_x$N films.

When the Co molar ratio is lower, the elements with larger atomic radii concentrate near the surface of the film but AlN, TiN and CrN concentrate near the surface, which causes the higher nanohardness of the film. With the increase in the Co element, the solid solution phase increases near the transition layer and AlN, TiN and CrN concentrate near the substrate of the film, which decreases the nanohardness of the film.

Figure 7 shows the adhesive force of NiTiAlCrCo$_x$N films. The adhesive force firstly increases and then decreases with the increase in Co content. When the Co molar ratio is 1.0, the film has a maximum adhesive force of 24.2 N. The reason is that AlN, TiN and CrN are concentrated near the substrate and have a better adhesive force with a TiN transition layer.

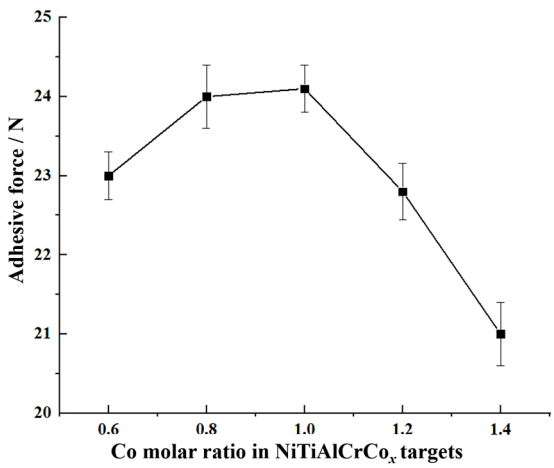

Figure 7. Adhesive force of NiTiAlCrCo$_x$N films.

3.4. Cavitation Erosion Resistance

Figure 8 shows the relationship between the mass loss and the cavitation erosion time of NiTiAlCrCo$_x$N films with different Co contents. The mass loss increases monotonically with the cavitation erosion time. The accumulative mass loss firstly decreases and then increases with the increase in Co content. When the Co content has a molar ratio of 1.4, the accumulative mass loss is the minimum of 0.72 mg and the cavitation erosion rate is of 0.12 mg/h.

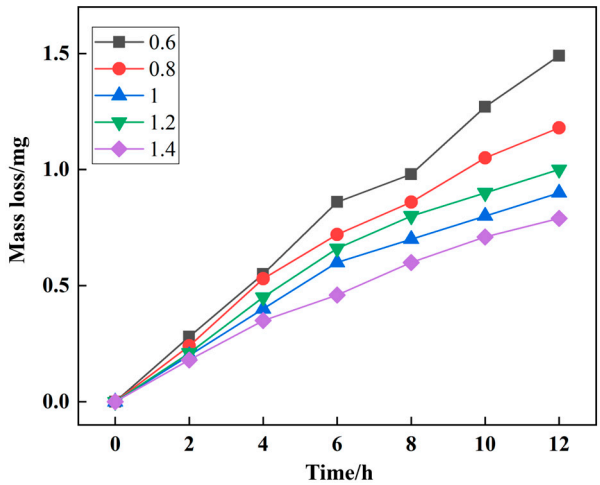

Figure 8. Mass loss curve of NiTiAlCrCo$_x$N films.

There are two reasons for the improvement in the cavitation erosion resistance of the films. First, when the Co content has a 1.4 molar ratio, the addition of the Co element enhances the solid solution strengthening effect [30]. Secondly, the film with the biggest elastic modulus has better elasticity to reduce the micro jet impact, which improves the cavitation erosion resistance of the film.

Figure 9 shows the surface and cavitation pits of NiTiAlCrCo$_x$N films after 12 h of cavitation erosion experiment. The film with a 0.6 Co molar ratio peels off. When the Co molar ratio is greater than 0.6, the films have no peeling, cracking or plastic deformation, and there are a few cavitation pits in the surface of NiTiAlCrCo$_x$N films. There is no rupture and spallation in NiTiAlCrCo$_x$N films, which implies a different cavitation mechanism from TiAlN and AlTiN films [31]. When the Co molar ratio is 1.4, the size of the cavitation pit is the minimum of 2.202 μm, which is consistence with the result seen in Figure 7.

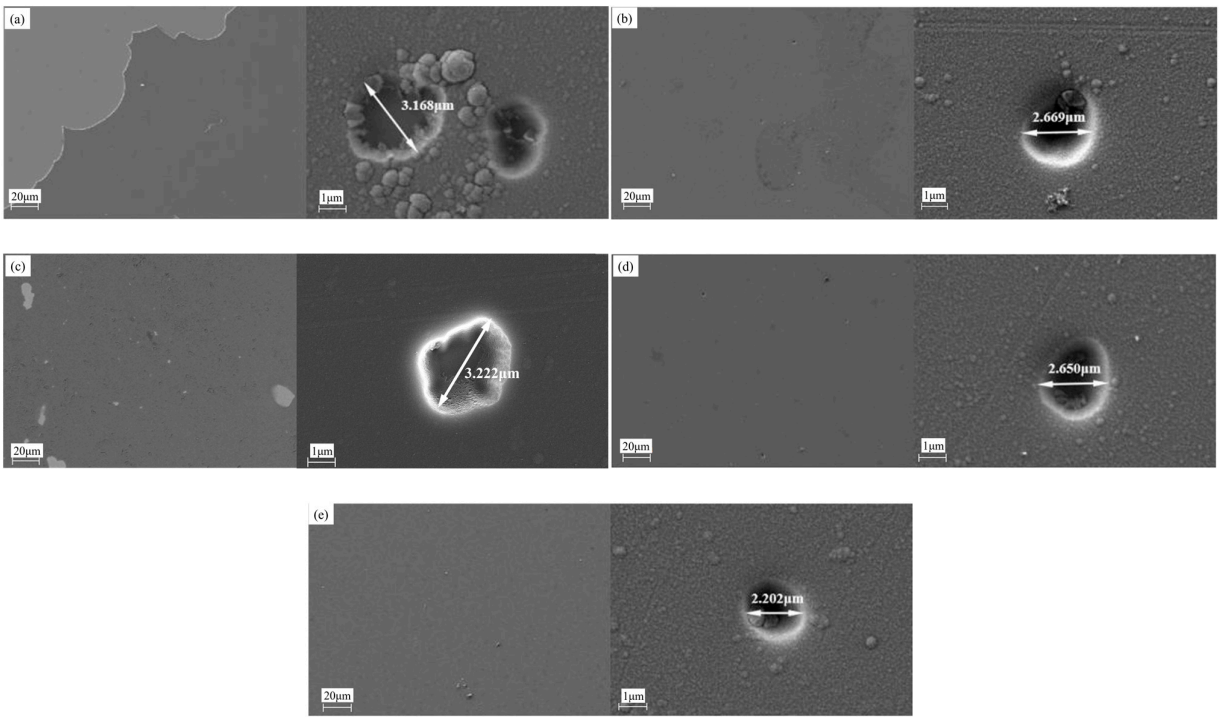

Figure 9. Surface and cavitation pit after 12 h cavitation erosion experiment. (**a**) NiTiAlCrCo$_{0.6}$N; (**b**) NiTiAlCrCo$_{0.8}$N; (**c**) NiTiAlCrCoN; (**d**) NiTiAlCrCo$_{1.2}$N; (**e**) NiTiAlCrCo$_{1.4}$N.

Figure 10 shows the element distribution of the cavitation pits of films with equimolar ratios. In the cavitation pit, Ni, Ti, Al, Co and N elements disappear and Cr and Fe elements appear, which means that the film undergoes breakdown and that the substrate of 304 stainless steel is exposed. The O element appears in the pit edge, which means that oxidations occur during the cavitation erosion. The Al, Co, N and O elements increase near the cavitation pits, which means that AlN, $Co_{5.47}N$ enriches near the surface of the films and reacts with O_2 to form Al_2O_3 and Co_2O_3 to resist the impact of micro jets. The addition of the Co element enhances the solid solution strengthening effect of the cavitation pits, which improves the cavitation erosion resistance of the films.

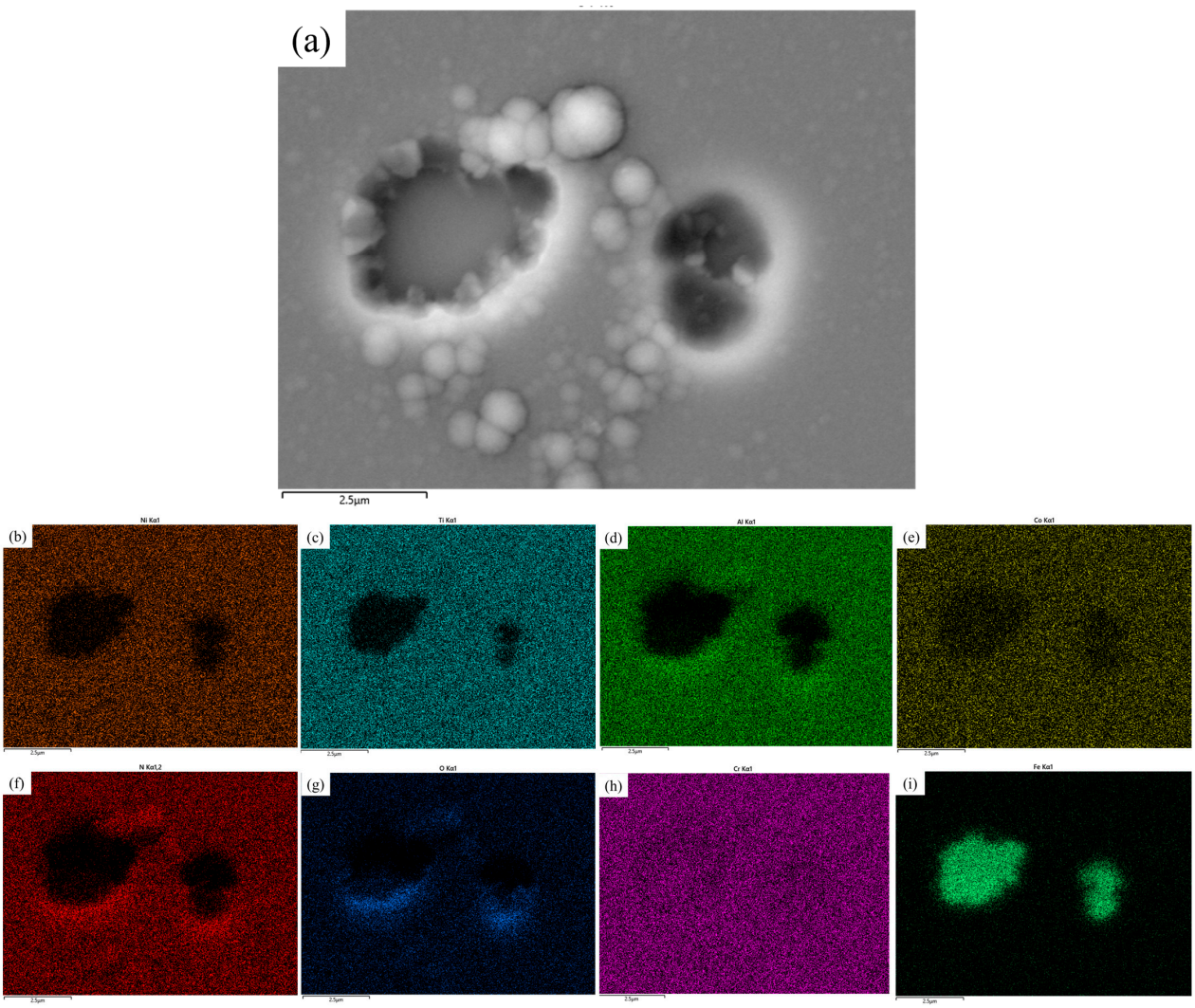

Figure 10. Element distribution of $NiTiAlCrCo_{0.6}N$ film cavitation pits. (**a**) Surface of cavitation pit; (**b**) Ni; (**c**) Ti; (**d**) Al; (**e**) Co; (**f**) N; (**g**) O; (**h**) Cr; (**i**) Fe.

4. Conclusions

The $NiTiAlCrCo_xN$ films with different Co contents were deposited on 304 stainless steel substrates by the magnetron sputtering system. The effect of Co content on microstructure and cavitation erosion resistance of the $NiTiAlCrCo_xN$ films was studied.

(1) The $NiTiAlCrCo_xN$ films with different Co contents have a simple face-centered cubic structure, and the preferred orientation appears on the (200) crystal plane. With the increase in Co contents, the interplanar spacing first increases and then decreases. The NiTiAlCrCoN film with equimolar ratios has the minimum interplanar spacing due to the lattice distortion effect and the slow diffusion effect.

(2) With the increase in Co content, the nanohardness of the $NiTiAlCrCo_xN$ films decreases and the elastic modulus of the $NiTiAlCrCo_xN$ films increases, expect for the ones of the $NiTiAlCrCo_{1.2}N$ film. The $NiTiAlCrCo_{1.4}N$ film has the lowest nanohardness of 13.264 GPa, and the highest elastic modulus of 253.22 GPa.

(3) The $NiTiAlCrCo_xN$ films have no peeling, cracks and plastic deformation, and there are few cavitation pits on the surface of the films, except for the $NiTiAlCrCo_{0.6}N$ film. The $NiTiAlCrCo_{x1.4}N$ film exhibits the minimum mass loss of cavitation erosion. There are two reasons for the improvement in the cavitation erosion resistance. Firstly, the addition of the Co element enhances the solid solution strengthening effect. Secondly, the $NiTiAlCrCo_{x1.4}N$ film with the biggest elastic modulus has better elasticity to reduce the micro jet impact, which improves the cavitation erosion resistance of the film.

Author Contributions: H.Y., F.C. and F.L. proposed the idea. F.C., L.S. and Y.Y. carried out the experiments. H.Y., F.C. and Z.D. analyzed the experimental results. H.Y. and F.C. wrote the main manuscript text. All authors have read and agreed to the published version of the manuscript.

Funding: This research was funded by National Natural Science Foundation of China (Grant No. U23A2025, 52305328), Natural Science Foundation of Beijing (Grant No. 3212003) and Yuyou Team of North China University of Technology (Grant No. 22XN746).

Institutional Review Board Statement: Not applicable.

Informed Consent Statement: Not applicable.

Data Availability Statement: All data are included in this published article.

Conflicts of Interest: The authors declare no conflicts of interest.

References

1. Wang, Y.; Hao, E.; An, Y.; Chen, J.; Zhou, H. Effects of microstructure and mechanical properties on cavitation erosion resistance of NiCrWMoCuCBFe coatings. *Appl. Surf. Sci.* **2021**, *547*, 149125. [CrossRef]
2. Wei, Z.; Wu, Y.; Hong, J.; Cheng, J.; Qiao, L.; Cheng, J.; Zhu, S. Ultrasonic cavitation erosion behaviors of high-velocity oxygen-fuel (HVOF) sprayed AlCoCrFeNi high-entropy alloy coating in different solutions. *Surf. Coat. Technol.* **2021**, *409*, 126899. [CrossRef]
3. Guan, Y.; Cui, X.; Chen, D.; Su, W.; Zhao, Y.; Li, J.; Li, X.; Feng, L.; Jin, G. Microstructure and properties analysis of FeCoNiAlCu dual-phase high-entropy alloy coating by laser cladding. *Surf. Coat. Technol.* **2023**, *467*, 129695. [CrossRef]
4. Luo, D.; Zhou, Q.; Huang, Z.; Li, Y.; Liu, Y.; Li, Q.; He, Y.; Wang, H. Tribological Behavior of High Entropy Alloy Coatings: A Review. *Coatings* **2022**, *12*, 1428. [CrossRef]
5. Huang, Y.; Hu, Y.; Zhang, M.; Mao, C.; Tong, Y.; Zhang, J.; Li, K.; Wang, K. On the enhanced wear resistance of laser-clad $CoCrCuFeNiTi_x$high-entropy alloy coatings at elevated temperature. *Tribol. Int.* **2022**, *174*, 107767. [CrossRef]
6. Xu, J.; Peng, S.; Li, Z.; Jiang, S.; Xie, Z.H.; Munroe, P.; Lu, H. Remarkable cavitation erosion–corrosion resistance of CoCrFeNiTiMo high-entropy alloy coatings. *Corros. Sci.* **2021**, *190*, 109663. [CrossRef]
7. Rong, Z.; Wang, C.; Wang, Y.; Dong, M.; You, Y.; Wang, J.; Liu, H.; Liu, J.; Wang, Y.; Zhu, Z. Microstructure and properties of $FeCoNiCr_x$ (x = Mn, Al) high-entropy alloy coatings. *J. Alloys Compd.* **2022**, *921*, 166061. [CrossRef]
8. Liu, Y.; Xiang, D.; Wang, K.; Yu, T. Corrosion of Laser Cladding High-Entropy Alloy Coatings: A Review. *Coatings* **2022**, *12*, 1669. [CrossRef]
9. Wu, X.; Lv, Y. Study on the Corrosion Resistance of Laser Clad Al0.7FeCoCrNiCux High-Entropy Alloy Coating in Marine Environment. *Coatings* **2022**, *12*, 1855. [CrossRef]
10. Lan, L.W.; Wang, X.J.; Guo, R.P.; Yang, H.J.; Qiao, J.W. Effect of environments and normal loads on tribological properties of nitrided $Ni_{45}(FeCoCr)_{40}(AlTi)_{15}$ high-entropy alloys. *J. Mate. Sci. Technol.* **2020**, *42*, 85–96. [CrossRef]
11. Straumal, B.; Rabkin, E.; Lopez, G.A.; Korneva, A.; Kuzmin, A.; Gornakova, A.; Straumal, A.; Baretzky, B. Grain boundary wetting phenomena in high entropy alloys containing nitrides, carbides, borides, silicides, and hydrogen: A review. *Crystals* **2021**, *11*, 1540. [CrossRef]
12. Pogrebnjaka, A.D.; Yakushchenkoa, I.V.; Abadiasb, G.; Chartier, P.; Bondar, O.V.; Beresnev, V.M.; Takeda, Y.; Sobol', O.V.; Oyoshi, K.; Andreyev, A.A.; et al. The effect of the deposition parameters of nitrides of high entropy alloys (TiZrHfVNb)N on their structure, composition, mechanical and tribological properties. *J. Super. Mater.* **2013**, *35*, 356–368. [CrossRef]
13. Lu, K.; Zhu, J.; Ge, W.; Hui, X. Progress on New Preparation Methods, Microstructures, and Protective Properties of High-Entropy Alloy Coatings. *Coatings* **2022**, *12*, 1472. [CrossRef]
14. Wang, Y.; Liu, S.; Dong, C. Research process and challenge of high entropy ceramic metarials. *J. Mater. Eng.* **2024**, *52*, 83–100.

15. Thorhallsson, A.I.; Fanicchia, F.; Davison, E.; Paul, S.; Davidsdottir, S.; Olafsson, D.I. Erosion and Corrosion Resistance Performance of Laser Metal Deposited High-Entropy Alloy Coatings at Hellisheidi Geothermal Site. *Materials* **2021**, *14*, 3071. [CrossRef]
16. Bao, Y.; Guo, L.; Zhong, C.; Song, Q.; Yang, K.; Jiang, Y.; Wang, Z. Effects of WC on the cavitation erosion resistance of $FeCoCrNiB_{0.2}$ high entropy alloy coating prepared by laser cladding. *Mater. Today Commun.* **2021**, *26*, 102154. [CrossRef]
17. Wu, C.L.; Zhang, S.; Zhang, C.H.; Zhang, H.; Dong, S.Y. Phase evolution and cavitation erosion-corrosion behavior of FeCoCrAlNiTix high entropy alloy coatings on 304 stainless steel by laser surface alloying. *J. Alloys Compd.* **2017**, *698*, 761–770. [CrossRef]
18. Baufeld, B. Effect of deposition parameters on mechanical properties of shaped metal deposition parts. *Proc. Inst. Mech. Eng. B-J. Eng.* **2012**, *226*, 126–136. [CrossRef]
19. Dai, C.D.; Fu, Y.; Guo, J.X.; Du, C.W. Effects of substrate temperature and deposition time on the morphology and corrosion resistance of $FeCoCrNiMo_{0.3}$ high-entropy alloy coating fabricated by magnetron sputtering. *Int. J. Miner. Metall. Mater.* **2020**, *27*, 1388–1397. [CrossRef]
20. Beresnev, V.M.; Nyemchenko, U.S.; Srebniuk, P.O.; Lytovchenko, S.V.; Sobol, O.V. Study of influence physical and technological parameters of deposition on the structure, physical and mechanical properties of vacuum arc coatings (Mo + Ti6%Si)N. In Proceedings of the 2016 International Conference on Nanomaterials: Application & Properties (NAP), Lviv, Ukraine, 14–19 September 2016.
21. Chen, L.; Li, W.; Liu, P.; Zhang, K.; Ma, F.; Chen, X.; Zhou, H.; Liu, X. Microstructure and mechanical properties of $(AlCrTiZrV)N_x$high-entropy alloy nitride films by reactive magnetron sputtering. *Vacuum* **2020**, *181*, 109706. [CrossRef]
22. Xu, Y.; Li, G.; Xia, Y. Synthesis and characterization of super-hard AlCrTiVZr high-entropy alloy nitride films deposited by HiPIMS. *Appl. Surf. Sci.* **2020**, *523*, 146529. [CrossRef]
23. Yan, H.; Liu, Y.; Mi, Z.; Si, L.; Dou, A.; Liu, F. Effect of nitrogen-argon flow ratio on cavitation resistance of NiTiAlCrN coating. *J. Func. Mater.* **2023**, *54*, 1007–1011.
24. Novikov, V.; Stepanov, N.; Zherebtsov, S.; Salishchev, G. Structure and properties of high-Entropy nitride coatings. *Metals* **2022**, *12*, 847. [CrossRef]
25. Zhou, C.; Wang, A.; Wang, G.; Zhang, J.; Liu, W. Investigation on the microstructure, wear and corrosion resistance of $FeCoNiCrMo_x$high-entropy alloy coatings deposited on 40Cr by laser cladding. *J. Mater. Sci.* **2022**, *57*, 18615–18639. [CrossRef]
26. Xiao, J.; Li, T.; Wu, Y.; Chen, J.; Zhang, C. Microstructure and tribological properties of plasma-sprayed CoCrFeNi-based high-entropy alloy coatings under dry and oil-lubricated sliding conditions. *J. Therm. Spray. Technol.* **2021**, *30*, 926–936. [CrossRef]
27. Sun, S.; Liu, H.; Hao, J.; Yang, H. Microstructural evolution and corrosion behavior of $CoCrFeNiAl_xMn_{(1-x)}$ dual-phase high-entropy alloy coatings prepared by laser cladding. *J. Alloys Compd.* **2021**, *886*, 161251. [CrossRef]
28. Ben, Q.; Zhang, Y.; Sun, L.; Wang, L.; Wang, Y.; Zhan, X. Wear and corrosion resistance of FeCoCrxNiAl high-entropy alloy coatings fabricated by laser cladding on Q345 welded joint. *Metals* **2022**, *12*, 1428. [CrossRef]
29. Yu, W.; Li, W.; Liu, P.; Zhang, K.; Ma, F.; Chen, X.; Feng, R.; Liaw, P.K. Silicon-content-dependent microstructures and mechanical behavior of (AlCrTiZrMo)-Si_x-N high-entropy alloy nitride films. *Mater. Design.* **2021**, *203*, 109553. [CrossRef]
30. Szala, M.; Chocyk, D.; Skic, A.; Kamiński, M.; Macek, W.; Turek, M. Effect of nitrogen ion implantation on the cavitation erosion resistance and Cobalt-based solid solution phase transformations of HIPed Stellite 6. *Materials* **2021**, *14*, 2324. [CrossRef] [PubMed]
31. Szala, M.; Walczak, M.; Pasierbiewicz, K.; Kamiński, M. Cavitation erosion and sliding wear mechanisms of AlTiN and TiAlN flims deposited on stainless steel substrate. *Coatings* **2019**, *9*, 340. [CrossRef]